ADVANCED INTELLIGENT SYSTEMS Open Access
www.advintellsyst.com

Scan and 3D Print: Magnetic Resonance Imaging-Guided, Monolithic Desktop Fabrication of Highly Biomimetic Skeletal System of the Human Hand

Gianni Stano, Matteo Cianchetti, Antonio Pavone, Mattia D'Orazio, Yonas Tadesse, and Gianluca Percoco*

3D-printed human-inspired hands, while visually similar to their biological counterparts, often lack key features that enable the unique capabilities of human hands. In this research, a framework for desktop 3D printing patient-specific human hands with a high functional level of biomimicry is presented. Magnetic resonance imaging (MRI) data are used to create computer aided design (CAD) models replicating key features of the skeletal system, including soft joints, ligaments, and volar plates, which are critical for mimicking the motions and functions of natural hands. The entire hand, consisting of rigid and soft segments, is monolithically 3D-printed using a commercial, inexpensive (≈€ 500) desktop multimaterial printer, eliminating the need for assembly and expensive 3D printers. The proposed MRI to Desktop 3D printing approach contrasts with the state of the art, where high biomimicry is achieved through a multistage assembly process and expensive 3D printing setups. The resulting hand shows several unique behaviors of natural hands, including an opposable thumb moving across the palm, improved resistance at bone–joint interfaces, high life cycle, constrained bending, absorption of perpendicular loads, high range of coordinated, bio-inspired motion, and grasping capabilities. The proposed approach can be potentially used to 3D print prosthetic hands tailored to individual needs, leveraging patient-specific digitally created MRI data.

1. Introduction

Additive manufacturing (AM) technologies have been extensively explored for fabricating human-inspired hands, offering significant advantages, such as cost-effectiveness, the ability to create intricate geometries, and the seamless integration of external elements. The primary AM technologies used in this domain include material extrusion (MEX), vat photopolymerization, and material jetting (MJ), as the mechanical properties of materials processed by these methods align closely with those of the structural components of human hands.[1–4]

Recent advancements have introduced features, such as electronic skins for proprioception and exteroception,[5–7] innovative control methodologies,[8] self-healing materials mimicking the reparative behavior of human skin,[9] and novel wearable actuators.[10,11] These developments are steering the design of 3D-printed hands toward a new paradigm. However, despite these innovations, current 3D printing technologies face significant challenges in producing highly biomimetic hands. Such hands must

G. Stano, A. Pavone, G. Percoco
Department of Mechanical
Mathematic and Management Engineering (DMMM)
Polytechnic University of Bari
Via E. Orabona 4, 70125 Bari, Italy
E-mail: gianni.stano@poliba.it

G. Stano, A. Pavone, M. D'Orazio, G. Percoco
Interdisciplinary Additive Manufacturing (IAM) Lab
TTEC- Taranto Polytechnic
Polytechnic University of Bari
Viale del Turismo 8, 74100 Taranto, Italy

The ORCID identification number(s) for the author(s) of this article can be found under https://doi.org/10.1002/aisy.202500470.

DOI: 10.1002/aisy.202500470

M. Cianchetti
The BioRobotics Institute
Scuola Superiore Sant'Anna
Viale Rinaldo Piaggio 34, 56025 Pontedera (PI), Italy

M. Cianchetti
Department of Excellence in Robotics and AI
Scuola Superiore Sant'Anna
Piazza Martiri della Libertà 33, 56127 Pisa, Italy

Y. Tadesse
Humanoids, Biorobotics and Smart Systems (HBS) Laboratory
Mechanical Engineering Department
The University of Texas at Dallas
Richardson, TX 75080, USA

replicate key human hand functions, including an opposable thumb, monodirectional finger bending, varied stiffness along the fingers (palmar and dorsal regions), robust soft–stiff interfaces, and human-like movement patterns.[4]

In scientific literature, three distinct approaches have been employed for fabricating 3D-printed hands. These approaches emerge from the interplay of three key factors: 3D printing cost, assembly complexity, and level of biomimicry. Each factor is categorized into two quantitative levels. The 3D printing cost is classified as either inexpensive (≤€ 5,000 for the printing setup) or expensive (>€ 5,000). The assembly complexity refers to the number of postprinting assembly steps, ranging from one-shot fabrication (0 assembly steps) to multiassembly (>1 assembly step). The biomimicry level is determined by the number of human hand features replicated, categorized as low (<2 features, typically bones and soft joints) or high (>3 features, including bones, soft joints, central slip, collateral ligaments, etc.). Based on these criteria, three fabrication approaches are defined: 1) cost-effective, monomaterial one-shot, low biomimicry, 2) expensive, multiassembly, high biomimicry, and 3) expensive, multimaterials one-shot, high biomimicry.

The cost-effective, monomaterial one-shot, low-biomimicry approach leverages the assembly-free nature of 3D printing, reducing fabrication time and eliminating assembly steps.[12,13] In this method, the movement of the fingers relies on engineered joints or hinges as described by Mutlu et al.[14] This approach is used in ref. [15] to monolithically fabricate a prosthetic hand with improved grasping capabilities only made of soft materials (thermoplastic polyurethane). Similarly, Zhou et al.[16] developed a 3D printed hand composed of thermoplastic polyurethane (TPU) for fingers and acrylonitrile butadiene styrene for the passive palm, where motion relies on the mechanical design of engineered joints rather than biomimicry. Deng and Tadesse[17] used the same one-shot approach for the fabrication of an entirely TPU-based hand, activated by means of custom-made and light-weight shape memory alloys (SMAs) actuators connected to tendons, in turn connected to every finger. Stiff materials, such as polylactic acid (PLA), have also been employed to fabricate hands featuring integrated complex mechanical mechanisms, including leaf springs and whippletree mechanisms, and a driving link, to provide motion (only bending) to the fingers.[18] It should be noted that selective bending was not allowed, as the main mechanism jointly pulled four fingers at the same time. De Pascali et al.[19] used a photopolymer flexible resin (shore A-85) to fabricate a soft hand with built-in pneumatic actuators, resulting in the on-demand bending of each finger. The monomaterial one-shot approach, despite being characterized by several advantages, such as reduced fabrication time and no assembly tasks, still suffers from low biomimicry, as it fails to replicate anatomical features like bone–joint systems, collateral ligaments, and volar plates, resulting in reduced functionality compared to human hands.

A different strategy involves the multiassembly high-biomimicry approach, where structural components of the hand are separately 3D-printed and subsequently assembled. This method allows for greater anatomical fidelity and improved hand functionality but requires many assembly tasks (and fabrication processes), resulting in increased fabrication time, higher labor costs, and potential inaccuracies or weaknesses at the assembly interfaces that could impact the overall performance and durability of the hand.

This approach was leveraged from Xu et al.,[20] they separately 3D-printed every single phalanx by using rigid material (preserving the original shape of the bones) and subsequently assembled them with flexible elements (no 3D printed) acting as joints and ligaments. By using this approach, an extremely high biomimicry degree was obtained, directly translated into replicating several human hand functions, such as complex finger motions, precision grasping, and repeatability of movements. Similarly, bones 3D printed from rigid materials and soft tissues 3Dprinted from soft materials have demonstrated the importance of biomimicry in successfully replicating human hand behaviors beyond mere finger bending.[21]

A third, still underexplored approach ("expensive multimaterial one-shot high biomimicry") consists of preserving biomimicry while leveraging one-shot 3D printing fabrication. However, this method usually comes with a price to pay: high cost of the 3D printing system, as MJ 3D printers can exceed 50 000 euros. Huges et al.[22] used a MJ Stratasys Connex 500 3D printer to jointly process soft and stiff materials in order to fabricate a highly biomimetic hand, composed of bones, soft joints, and collateral ligaments. The 3D-printed hand was passively used by exploiting the anisotropic stiffness of the bone–joint configurations for playing piano. According to this approach, Buchner et al.[23] advanced the soft–stiff 3D printing paradigm by using a vision-controlled MJ 3D printing setup to fabricate a highly bioinspired 3D printed hand comprising rigid bones, soft joints, thereby enhancing both biomimicry and functionality.

This approach, while associated with significant costs, remains the only state-of-the-art method capable of fabricating bioinspired hands in a single manufacturing step without the need for assembly tasks, thus achieving a seamless integration of structural and functional elements.

This article introduces a fourth unexplored approach, which combines low-cost, one-step fabrication and high biomimicry, leveraging an inexpensive desktop multimaterial MEX 3D printer (≈€ 500) for the monolithic fabrication of highly biomimetic hands. The proposed method incorporates magnetic resonance imaging (MRI)-guided design to include often-overlooked anatomical elements, such as volar plates and collateral ligaments, which significantly enhance biomimicry and functionality by enabling constrained bending and reducing lateral translation. Key features of the proposed hand include a tougher soft–stiff interface, achieved through a gradient generation technique at the soft–stiff interface, and bioengineered 3D interlocks that relocate rupture points away from the interface, mimicking biological systems. Additionally, the MRI-based design enables a wide range of bioinspired motions, including an opposable thumb moving across the whole palm capable of opposing all the other four fingers, and abduction capability, which translates into the possibility of performing either power or precision grasping. The authors envision the proposed method enabling the desktop 3D printing of assembly-free, cost-effective devices for customized prosthetic hands tailored to individual needs, using patient-specific digital models derived from MRI data. In a future where digital twins of human bodies are widely available, this approach could facilitate the reproduction of body parts with biomechanical properties nearly identical to the originals.

Such advancements hold significant implications for prosthetics, offering improvements in functionality, production efficiency, customization, and accessibility.

2. Results

2.1. MRI to One-Shot Desktop Fabrication of Human-Inspired Hand

3D-printed robotic hands often lack key features that enable the unique functionalities of human hands, such as an opposable thumb, shock absorption under perpendicular loads, prevention of finger hyperextension in unintended directions, and more. To address these limitations and preserve the geometric and shape fidelity of human fingers, this research utilized MRI data to create CAD models. These models incorporate rigid bones, soft joints, and essential soft components, such as the volar plate and collateral ligaments, which are typically excluded in robotic hand designs. More details about the CAD models starting from MRI are provided in the Experimental Section. An inexpensive desktop multimaterial 3D printer (≈€ 500) was employed to fabricate both rigid and soft segments, in a single shot. In addition, a custom gradient generation technique was developed via.gcode modification to enhance adhesion at the soft–stiff interface. This was complemented by engineered interlocking features, which improved interfacial adhesion by 293% and relocated the rupture site away from the interface, mimicking failure behavior observed in biological systems. This monolithic 3D-printing approach eliminates the need for assembly steps, producing a fully functional structure immediately upon removal from the printer. Otherwise, assembling the 27 bones[24] of the human hand itself would require an extremely intricate and time-intensive process. The resulting hand demonstrates a high degree of biomimicry, unlocking the rigorous replication of several behaviors of human hands, including constrained bending, lateral shock absorption of the finger, opposable thumb, abduction, and bioinspired motions when activated.

The workflow for this research is depicted in **Figure 1**A, illustrating the combination of two key elements: 1) an MRI-CAD framework and 2) a multi-MEX 3D printing paradigm. As shown in Figure 1B, this unique approach achieves a high degree of biomimicry through a streamlined, cost-effective monolithic fabrication process utilizing a desktop multimaterial MEX system. This contrasts with existing literature, where high biomimicry is typically achieved through multiple assembly steps, and one-shot fabrication methods often result in low bioinspired designs, or alternatively, extremely expensive MJ 3D printing machines are required for fabricating assembly-free hands with high biomimicry.

The primary advantage of this method lies in its elimination of assembly steps (see Figure 1C) while simultaneously enhancing the biomimicry of the 3D printed hand, leveraging an inexpensive multimaterial MEX desktop setup. In addition to the cost-effectiveness of the 3D printing setup, the estimated cost of the entire hand is € 9.37 (see Section S1, Supporting Information), making the proposed approach accessible to a broad audience. A total time of 17 h and 20 min was needed for the whole fabrication and postprocessing of the proposed hand. With a digital twin of the hand (CAD model based on MRI data), the proposed method allows efficient manufacturing of exact replicas of motor functional elements of hands or fingers for either prosthetic purposes or physical twins, tailored to the specific person. As a matter of fact, scalability is a key feature of the proposed method (see Figure 1D): the inexpensive multimaterial desktop 3D printer employed offers high resolution (12 μm) and accuracy (1 μm), enabling the fabrication of fine anatomical details in downsized models (e.g., a one-year-old's hand). Additionally, its ample build volume (300 × 300 × 340 mm) allows manufacturing large models, such as those representing individuals up to 200 cm in height. Movie S1, Supporting Information, shows the proposed multimaterial 3D printed hand performing human-like movements.

Beyond the significant reduction in 3D printer cost (≈€ 500 for MEX compared to over € 10 000 for MJ), the proposed hand fabricated via MEX offers several key advantages over state-of-the-art hands produced using MJ techniques. These advantages primarily lie in the broader range of printable materials, exhibiting an elongation at break of up to 600% with MEX, compared to 250% for MJ, and in the superior adhesion strength at soft–stiff interfaces (38 MPa in this work versus 1.8 MPa for MJ[23]). These improved material characteristics, combined with the anatomical accuracy enabled by the proposed MRI-informed design framework, lead to significantly enhanced biomechanical performance, including increase in palmar stiffness (114.9 $N\,m^{-1}$ against 50 $N\,m^{-1}$[22]), lateral stiffness (1835 versus 100 $N\,m^{-1}$[22]), and improved thumb mobility (Kapanji score of 10 versus 6[23]). A detailed quantitative comparison between the proposed MEX-fabricated hand and MJ-based counterparts is provided in **Table 1**.

The MRI-to-3D print method presented in this research represents a first step toward a new intelligent digital manufacturing approach of soft–stiff musculoskeletal systems aimed at enhancing their functionality and performance through two main cores: 1) AM, and 2) bioinspiration.

2.2. Creating Tougher Soft–Stiff Interfaces

In biological systems, soft–stiff interfaces represent the toughest part of the musculoskeletal systems, hardly ever do failures happen at the interface.[25,26] However, in 3D-printed soft–stiff interfaces, the behavior is the opposite, these interfaces often represent the weakest points, prone to rupture due to localized stress concentrations.

In scientific literature, the selection of rigid and soft materials for fabricating 3D-printed hands is primarily guided by the mechanical properties of the materials. Polymers and composites with Young's modulus, ultimate tensile strength (UTS), and elongation at break values close to those of human counterparts are typically chosen. In this research, a novel adhesion-oriented metric was employed to optimize material selection for soft–stiff interfaces, prioritizing adhesion performance over standalone mechanical properties.

A total of four rigid materials, with properties comparable to finger bones, and two soft materials, mimicking the mechanical behavior of soft joints, were considered. Details about these material groups are provided in Section S2, Supporting Information. All possible combinations of these materials were tested mechanically (three repetitions per combination) following the procedure described in the Experimental Section.

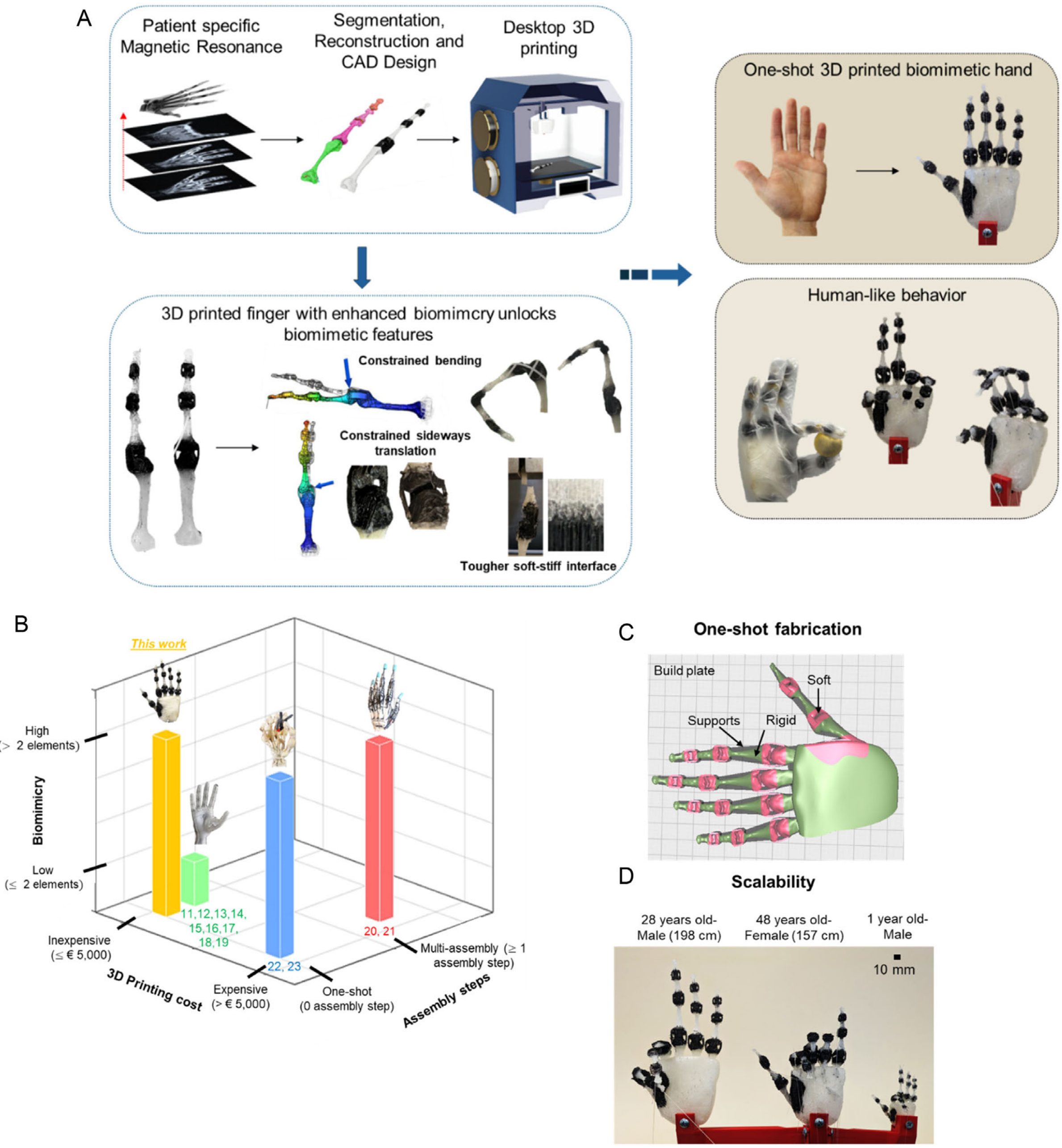

Figure 1. One-shot desktop 3D printing of the proposed biomimetic hand using MRI data. A) Workflow underlying the present research. It should be noted that white color represents bone-like segments (stiff materials), while black color represents joint-like segments (soft material); and B) state of the art in 3D printed hands, and positioning of the proposed work. As described in the Introduction section, three main patterns characterize 3D printed hands: i) green bar: cost-effectiveness, monomaterial one-shot, low-biomimicry, ref. [15]. ii) red bar: multiassembly, high biomimicry, ref. [20] and iii) blue bar: expensive, multimaterial one-shot, high biomimicry, ref. [23]. The present paper aims at creating a new paradigm (yellow bar): cost-effectiveness, multimaterial one-shot, and high biomimicry by using desktop multimaterial MEX and MRI-guided design. C) Proposed hand in the slicing software for one shot 3D printing, D) Scalability of the proposed MRI-desktop 3D printing approach.

Among the tested combinations, PLA and soft TPU 85 A (TPU 85 A) showed the highest adhesion strength, as illustrated in **Figure** 2A,B. Their adhesion was four times higher than the adhesion of the unoptimized combination, including carbon fiber nylon (often used to 3D print bones, as its mechanical performances are better compared to other materials when considered as a stand-alone material) and TPU 75 A. Although the analysis was conducted on plain interfaces (no interlocking), a graded region was introduced at the soft–stiff interface, inspired by biological systems where soft and stiff materials transition through a gradient composed of both materials.

Creating a graded region has been shown to enhance adhesion.[27–29] However, conventional techniques typically require either external custom mixing devices integrated into

Table 1. Comparison between MJ-fabricated hands and proposed MEX-fabricated hand.

	MJ-fabricated ref. [22]	MJ vision jet-fabricated ref. [23]	Proposed work	Comments
3D printer	Stratasys Connex 500	InkBit Vista	JG Maker Artist D Pro	n/a
Cost of 3D printer	Around € 35 000	Around € 500 000	Around € 500	n/a
Soft material (elongation at break)	220%	250%	600%	Possibility to use more flexible materials in MEX
Soft–stiff interface adhesion	n/a	1.8 MPa	38.6 MPa	Improved soft-stiff adhesion
Kapandji test (thumb opposability)	n/a	6 out of 10	10 out of 10	Improved range of motions
Adduction/abduction	Allowed	n/a	Allowed	n/a
Stiffness of the finger (palmar)	50 N m^{-1}	n/a	114.9 N m^{-1}	Higher palmar stiffness prevents unwanted backward bending
Lateral stiffness	100 N m^{-1}	n/a	1835 N mm^{-1}	Effect of the volar plate - prevents unwanted sideways bending

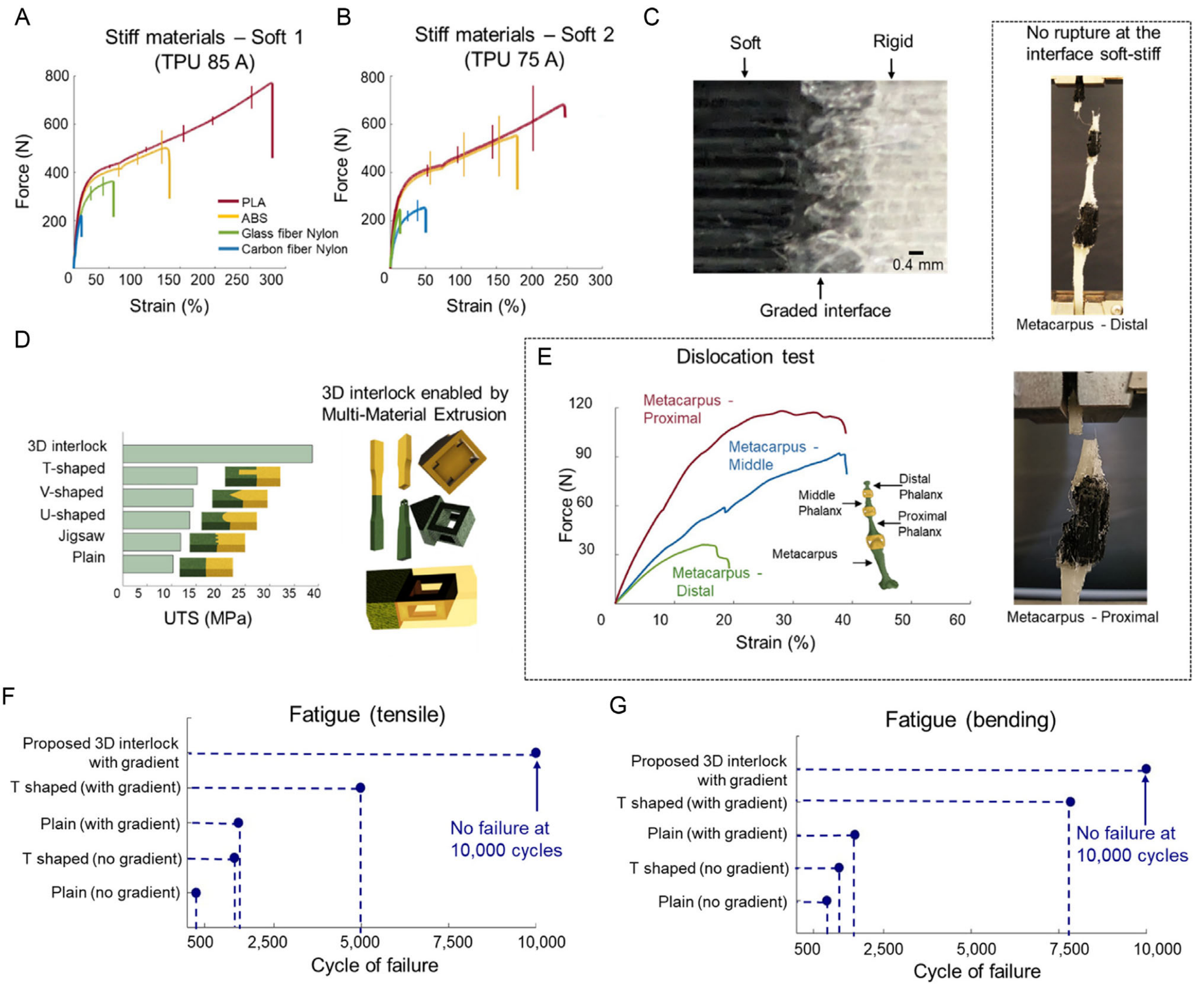

Figure 2. Adhesion-centered material selection for tougher soft–stiff interfaces. A) Adhesion results for stiff materials and soft material 1 (TPU 85 A); B) adhesion results for stiff materials and soft material 2 (TPU 75 A); C) graded soft–stiff interface generated via the proposed gradient generator technique; D) effect of interlocking on the interface adhesion; E) dislocation test on 3D printed finger, showing that no rupture occurred at the interface; F) fatigue test under tensile loading; and G) fatigue test under bending loading.

the 3D printer[30,31] or custom-designed digital filaments.[32] While highly effective, these methods are challenging to implement for a broader audience as they necessitate significant modifications to the 3D printing setup.

To overcome these limitations, the authors employed a gradient generation technique that requires only G-code modifications, eliminating the need for hardware alterations. This method utilizes a custom script to overlap the soft material onto the rigid material at the interface at every extruded layer, forming a material gradient. After extruding a plain soft–stiff interface, the nozzle is instructed through.gcode modification to extrude an extra amount of soft material (0.4 mm wide and 0.2 mm thick) directly on top of the rigid one, to create an overlap region. Immediately after creating the overlap region (before starting printing the next layer), the hot nozzle performs an ironing process on the interface, applying both pressure and localized reheating to enhance wettability and molecular interdiffusion,[33] thereby resulting in improved interfacial bonding.[34,35] The ironing process diffuses the soft material within the rigid one: a strain interface gradient is introduced. In summary, the proposed gradient generation technique is based on two fundamental consecutive steps happening at the interface: i) extrusion overlap, and ii) ironing process.

The proposed technique increased adhesion by 37.8% and was adopted throughout the whole study. Further details are provided in the Experimental Section and in Figure S1B, Supporting Information. Figure 2C shows the soft–stiff interface manufactured with the proposed gradient generation technique.

After finding the most suitable pair of stiff–soft materials on plain interfaces with a graded transition region, the mechanical interlocking method, widely recognized to improve interface adhesion between dissimilar materials, was leveraged. Traditional 2D interlocking designs were evaluated, with the T-shaped interlock demonstrating the highest improvement in UTS, increasing from 9.8 MPa (plain interface) to 15.2 MPa. Inspired by the principle that increased contact area along 3-dimensions enhances adhesion,[36] a custom 3D interlocking mechanism was developed (see Figure 2D). Unlike conventional 2D mechanisms, this design provides additional contact along the third dimension, enabled by MEX technology, which would be challenging to achieve using traditional manufacturing methods. The proposed 3D interlocking mechanism yielded a UTS of 38.6 MPa, representing a 293% increase compared to the plain interface (often used when 3D printing soft–stiff interfaces) and a 153% improvement over the best 2D interlock (T-shaped). This interlocking approach was integrated into the CAD design of the finger model, based on MRI data: each phalanx-joint system included an embedded internal 3D interlock.

To evaluate the performance of the 3D interlocking mechanism, dislocation tests were conducted on 3D-printed fingers (Figure 2E). During these tests, each phalanx was pulled individually while the metacarpus was fixed. As shown in Figure 2E and Movie S2, Supporting Information, failures consistently occurred within the phalanx material rather than at the interface. This outcome demonstrated that the soft–stiff interface was tuned to be tougher than the bone itself, as found in biological systems. Notably, when the proximal phalanx was pulled while the metacarpus was fixed, a force of 117 N was required to induce failure. The entire finger exhibited an elongation at break of 37%, further validating the robustness of the interface and the effectiveness of the proposed 3D interlocking mechanism.

The proposed 3D interlocking soft–stiff gradient interface was evaluated under repeated loading conditions. Two low-frequency fatigue tests, one in tension and one in bending, were conducted to benchmark the performance of the proposed interface against conventional designs. Details of the testing protocols are provided in the Experimental Section. In both tests, the 3D gradient interface withstood all 10 000 loading cycles without failure, whereas traditional interfaces failed between 383 and 7,748 cycles (See Figure 2F,G). These results demonstrate that the proposed interface is not only mechanically tougher and capable of relocating the failure point away from the interface but also exhibits superior fatigue resistance. This makes it a highly promising solution for musculoskeletal applications, where durability under cyclic loading is critical. Future work will focus on a more in-depth characterization of the proposed interface, including its performance under varying environmental conditions such as temperature and humidity.

2.3. Unlocking Human Finger Behavior: Volar Plate and Collateral Ligament

The proposed 3D-printed finger (see **Figure 3**A) is equipped with two key elements, often omitted in 3D-printed robotic hands: collateral ligament and volar plate. These components enable unique functionalities rarely reported in robotic musculoskeletal systems. As illustrated in Figure 3B,C, the volar plate plays a crucial role in ensuring directional bending of the finger. When a force is applied to the dorsal (nail) side of the finger, the volar plate permits bending in the direction of the applied force. Conversely, when a force is applied to the palmar side, the volar plate acts as a constraint, preventing bending in the opposite direction. This feature is vital for avoiding abnormal hyperextension of the finger and ensures that the finger bends only in one direction, mimicking natural human behavior. This functionality is particularly advantageous when grasping heavy loads, as it prevents unintended bending, improves stability, and evenly distributes forces. This enhances the finger's load-bearing capacity and reliability in demanding applications. The proposed finger, unlike 3D printed fingers found in scientific literature, is characterized by two distinct stiffness values: low stiffness on the dorsal side and high stiffness on the palmar side. A direct comparison between the stiffness (palmar side) of the proposed finger with some relevant works on 3D-printed fingers[14,37] found in literature is provided in Section S3, Supporting Information.

As shown in Figure 3D,E, the collateral ligament is critical for maintaining joint stability and functionality. When a force perpendicular to the finger's central axis (radial side) is applied, the collateral ligament absorbs stress, preventing abnormal lateral movements. Without this component, the finger would experience undesired sideways motions, leading to joint instability during flexion and extension.

Both elements were characterized, proving their importance and the direct correlation between biomimicry and human-like behavior. As shown in **Figure 4**A,B, a force of 3 N applied to the dorsal side (natural bending direction of human fingers) resulted in a maximum vertical displacement of 43.8 mm. In contrast, the

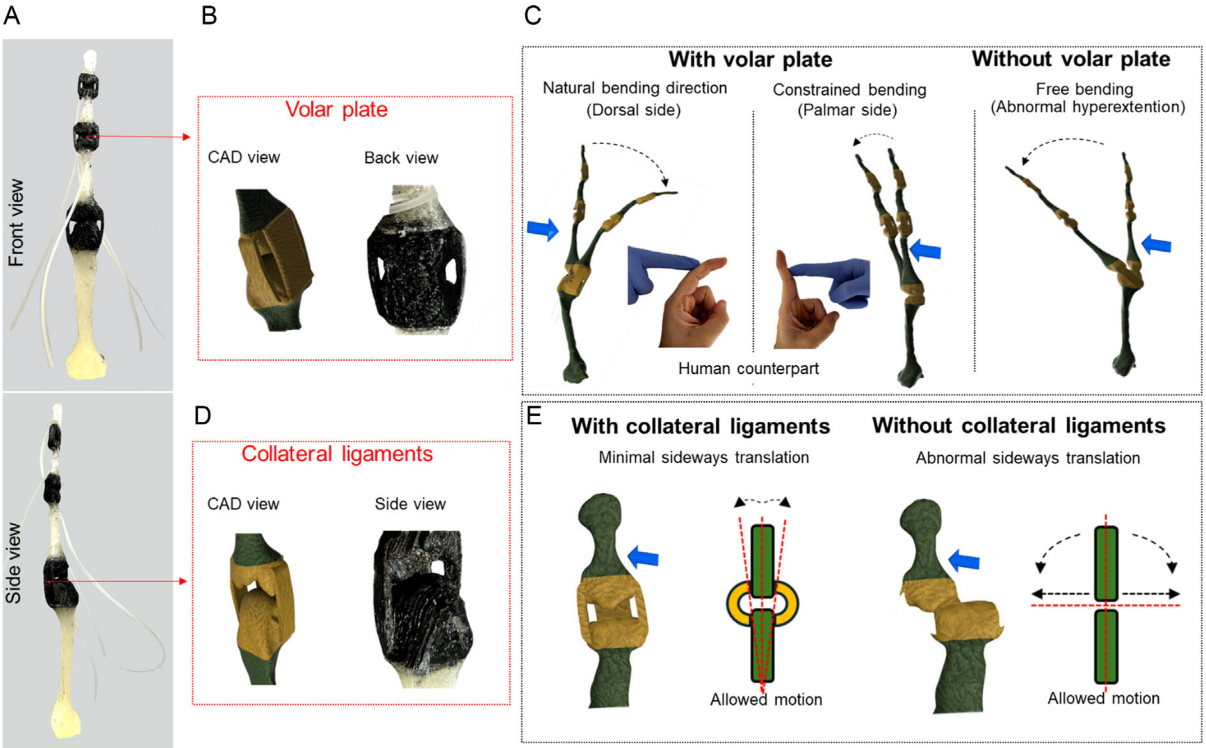

Figure 3. Key biological elements embedded into the proposed finger: the volar plate and collateral ligament. A) One-shot 3D printed finger, B) 3D-printed volar plate, C) effect of volar plate, D) 3D-printed collateral ligament, and E) effect of collateral ligament.

same force applied to the palmar side yielded a maximum vertical displacement of 26.1 mm. The influence of the volar plate[38] is further evident in the stiffness of the proposed finger, which was calculated as follows

$$S = \frac{F}{d} \tag{1}$$

where S is the stiffness (N m^{-1}), F is the maximum force applied (N), and d is the maximum vertical displacement of the tip (m). A dorsal and palmar stiffness of 68.5 and 114.9 N m^{-1} were achieved, respectively. It should be noted that the volar plate increases the stiffness of 67.7% on the palmar side, thereby providing high load-bearing capacity to the finger, preventing the abnormal hyperextension when loads are applied in the palmar direction (see Movie S3, Supporting Information). These results also closely align with the findings of[39] which reported a mean human finger displacement of 3.7 mm at a force of 1 N applied to the dorsal side. In comparison, the proposed 3D-printed finger exhibits a vertical displacement of 4.1 mm under the same loading condition. This similarity highlights the effectiveness of the proposed MRI-informed framework in replicating human finger behavior, particularly within the force range of 0 to 3 N, which is typical in real-world scenarios.

The collateral ligament was tested by applying a maximum force of 10 N on the radial side: under this condition, the fingertip exhibited a maximum displacement of 5.45 mm, as shown in Figure 4C,D. It should be noted that a force of 6.2 N is required to obtain a minimum lateral translation of the tip of 0.2 mm. Below that threshold, no lateral translations were detected. The collateral ligament provided high structural integrity to the finger, mimicking the human finger counterpart, as shown in Movie S4, Supporting Information. A lateral stiffness of 1835 N m^{-1} was achieved in the proposed 3D-printed finger due to the contribution of the collateral ligament. This value is comparable to the experimentally measured lateral stiffness of 2700 N m^{-1} reported in ref. [39] based on tests conducted on 20 human subjects. The authors attribute the reduced stiffness in the present model to two main factors: i) the measurements in ref. [39] were performed on real fingers, which include skin and other biological tissues that contribute to increased stiffness, unlike the proposed 3D printed finger, which consists solely of bones and soft joints; and ii) the experimental data in ref. [39] reflect intersubject variability, as the cohort included individuals of varying age, weight, and height. The testing procedure used for both the volar plate and the collateral ligament is detailed in the Experimental Section.

The behavior exhibited when testing both the volar plate and the collateral ligament (incorporated into the finger design thanks to the proposed MRI-guided approach) was accurately predicted by simulations, using elastic and hyperelastic models (see Section S4, Supporting Information). The tip displacement was predicted with an accuracy of 95.6%, 98.2%, and 96.3% when applying force on the dorsal side, palmar side, and radial side, respectively. Such a tool could also be potentially used to perform topological optimization, further enhancing the positive effects of the volar plate and collateral ligaments under specific conditions (i.e., high loads, fatigue, and others).

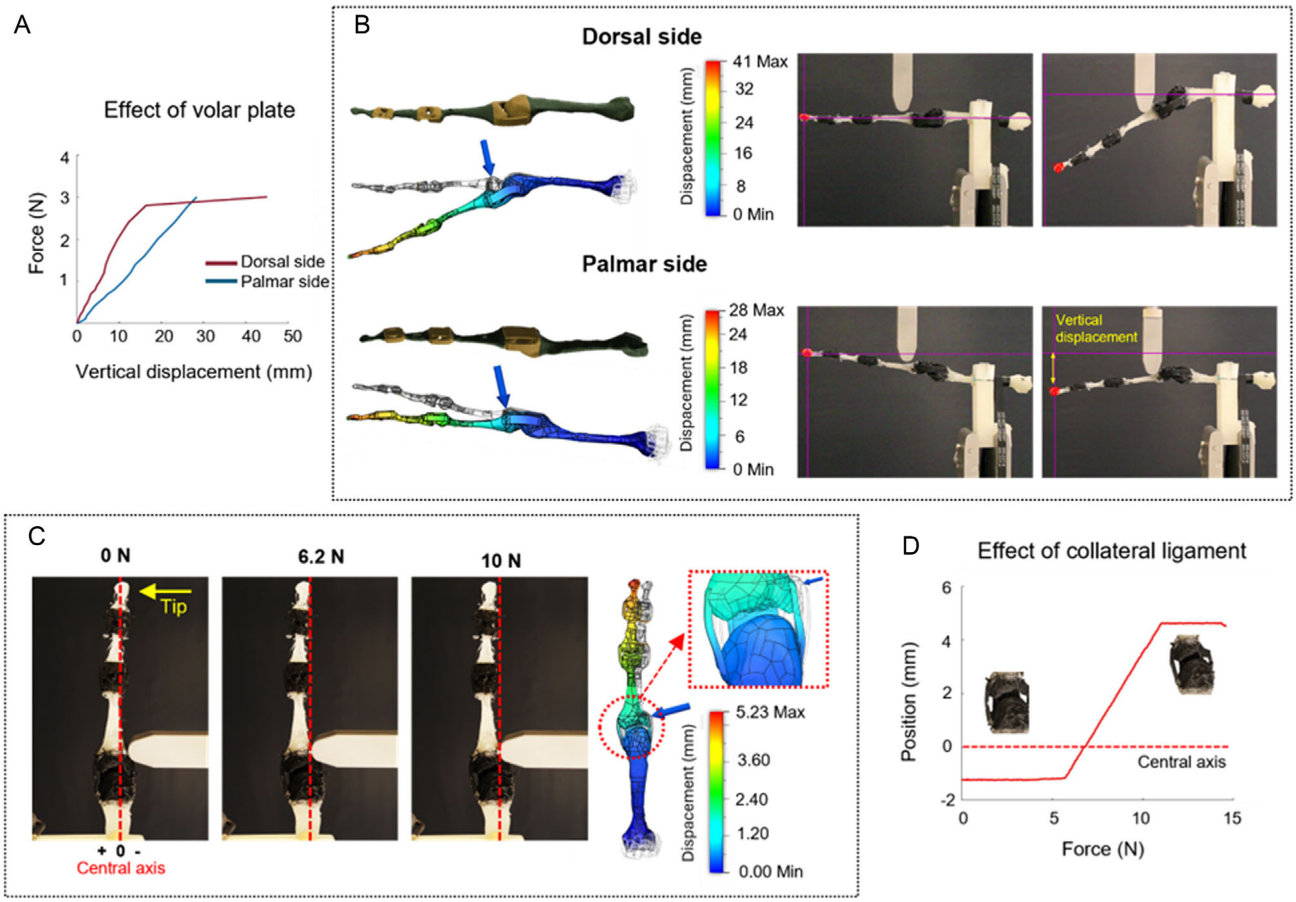

Figure 4. Characterization of 3D-printed biological elements: A) Effect of volar plate on fingertip displacement; B) volar plate on dorsal side and palmar side bending during the test, benchmarked with FEM simulations; C) collateral ligament in minimizing the lateral translation during the test, benchmarked with FEM simulations; and D) effect of collateral ligament on lateral translation.

2.4. 3D-Printed Hand Motion Capabilities

In this section, the motion capabilities of the proposed 3D-printed hand are characterized and analyzed. The robotic hand utilized a tendon-driven actuation system, where a NEMA 17 stepper motor (1.8° step angle, 200 steps/rev) controlled the tension of a 0.4 mm diameter nylon tendon (200 mm length), wrapped around a 10 mm diameter pulley.

A first motion analysis was performed on a stand-alone finger (index) to evaluate the range of motions enabled by the proposed design. Three pulling magnitudes were evaluated, namely low, medium, and high, characterized respectively by 100, 300, and 600 steps. The three different pulling magnitudes, resulting in an estimated force of 5 N, 15 N, and 30 N (assuming a proportional torque distribution with the number of steps), are represented in **Figure 5**A by three different sizes of triangles.

As shown in Figure 5A, several bioinspired motions of the fingers can be achieved as a combination of the activated tendon and pulling magnitude, thereby resulting in a wide range of motions resembling the human counterpart. In particular, several values of bending angle of the tip (calculated with respect to the finger central axis) are achieved, spanning from a minimum of 5.8° to a maximum of 90°.

Motion repeatability was evaluated for a total of six configurations (every configuration is based on the activation of specific tendons at specific activation magnitude values; each configuration was repeated 30 times with 2 s rest intervals between activations). The fingertip positions in 2D space for each configuration are shown in Figure 5B, demonstrating a low standard deviation (always lower than 7 mm in both x- and y-axis, see Section S6, Supporting Information), confirming finger robustness, constant kinematics, and suitability for repetitive movements.

The proposed one-shot 3D-printed hand is characterized by a feature often overlooked in 3D-printed inexpensive hands, but beneficial for grasping and prosthetic applications: the opposable thumb. As shown in Figure 5C, when activated, the thumb exhibits a behavior close to the human counterpart in terms of opposability (see Movie S5, Supporting Information). Figure 5C demonstrates that, depending on the pulling magnitude and the activated tendons, the thumb can move across the palm, emulating natural motions. A total of six configurations (defined by the pulling magnitude: steps ranging from 50 up to 400) were analyzed and repeated a total of 30 times, resulting in high repeatability as the standard deviation is always lower than 0.42 cm in both x- and y-axis (see Section S6, Supporting Information). Furthermore, the Kapandji test was performed

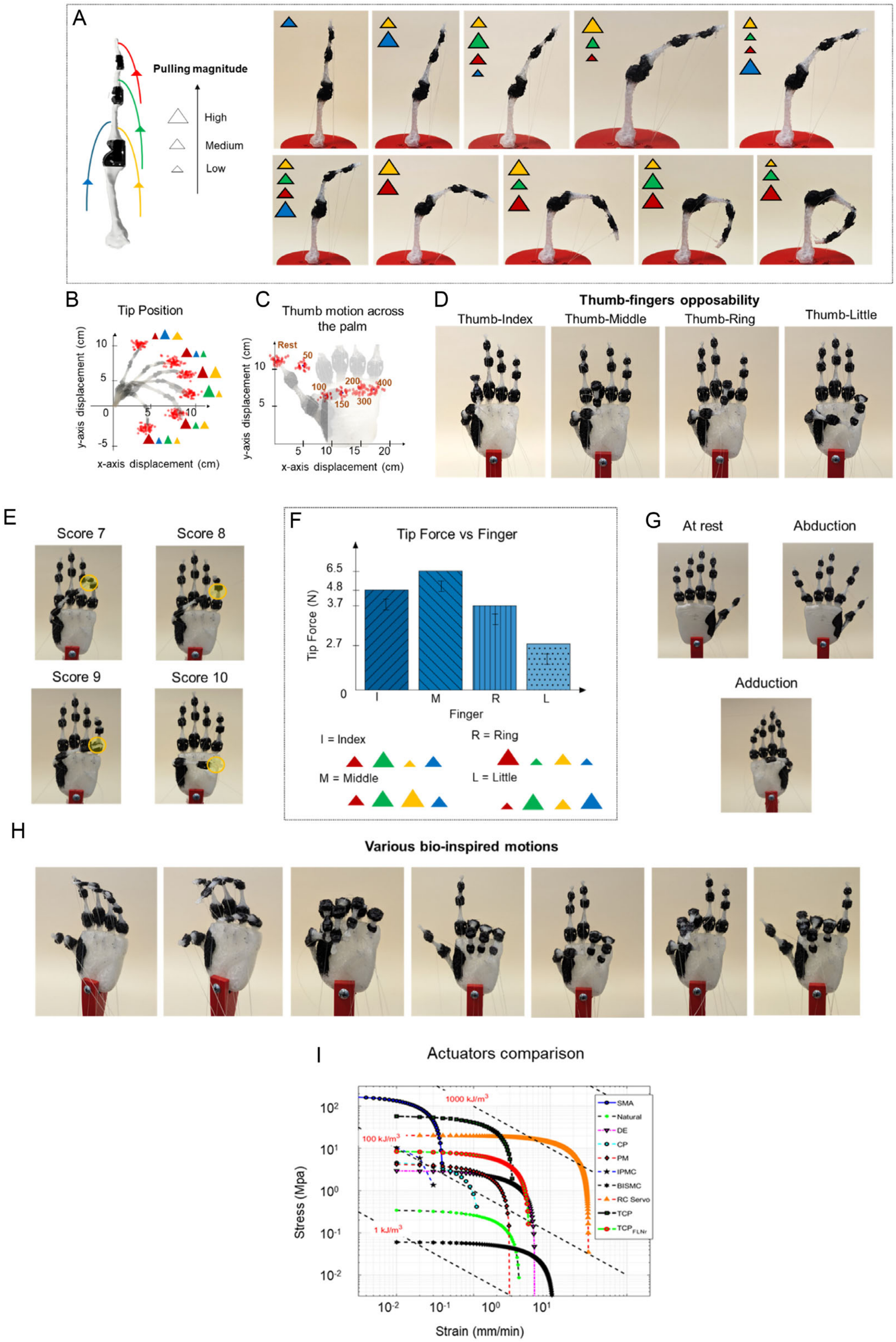

Figure 5. 3D-printed finger and hand: A) Several human-like motions exhibited by the proposed 3D printed finger, based on the activated tendons and pulling magnitude; B) index finger repeatability test: every motion configuration (six in total) was repeated 30 times with intervals of 2 s between two consecutive activations; C) repeatability test for the opposable thumb moving across the palm; D) Kapanjii test showing the thumb fingers opposability; E) Kapanjii test: score 7, 8, 9, and 10; F) blocking force of index, middle, ring, and little finger activated under specific conditions (pulling magnitude); G) abduction of the proposed hand; H) several bioinspired motions, and I) comparison among commonly used artificial muscles in terms of stress, strain, and power density.

by consecutively opposing the thumb to the other four fingers (see Figure 5D): the thumb tip–finger tip contact was evaluated. After defining the correct step setting for every configuration, the opposability was evaluated by simultaneously activating the thumb and one other finger per time (from index to little finger) for a total of 30 consecutive time, resulting in a tip opposition (contact between the tips of the thumb and the finger) success rate of the 100% for all the four configurations. Beyond thumb-finger opposability, the Kapandji tests highlighted the full potential of the proposed hand design. As illustrated in Figure 5E, a score of 10 (the highest possible) was achieved. Specifically, the thumb was successively opposed to the following points on the little finger: the distal interphalangeal (DIP) joint (score 7), the proximal interphalangeal (PIP) joint (score 8), the metacarpophalangeal joint (score 9), and the distal palmar crease (score 10).

Future tests will focus on the complete characterization of thumb behavior, replicating several human behaviors beyond pure opposability, such as rotation (circumduction).

The tip force of the index, middle, ring, and little fingers was characterized under specific conditions. For each finger, a unique movement configuration, defined by the combination of pulled tendons and pulling magnitude (motor torque), was analyzed, as illustrated in Figure 5F. It should be noted that during the force test, only one finger at a time was activated. Each movement configuration was arbitrarily chosen, and the corresponding finger movement was repeated 30 times. As shown in Figure 5F, the higher blocking force was achieved with the middle finger (6.5 N), while the lower was with the little finger (2.7 N), as expected. Moreover, the standard deviation of the measured forces was lower than 0.6 N for all values of force, demonstrating the robustness of the proposed hand design.

Details of the experimental setup for measuring the tip force are provided in Section S7, Supporting Information.

In addition, the MRI-guided framework enables the replication of human soft joints, including both the volar plate and collateral ligaments: key anatomical features that allow lateral finger abduction. This movement is crucial in human hand function, as it enhances the ability to grasp and manipulate objects of varying shapes and sizes. During the fabrication process, the dorsal interosseous tendons were embedded on the dorsal side of both the index and little fingers, along with the other tendons, illustrated in Figure 5A. Upon activation, finger abduction was successfully achieved, as shown in Figure 5G. Specifically, the central axis of the index finger translated by 24 mm, while that of the little finger translated by 38 mm, following a tendon actuation of 500 steps. The overall hand span, measured from the tip of the index finger to the tip of the little finger, increased from 62 mm at rest to 126 mm upon activating the dorsal interosseous tendons of both fingers. This behavior, made possible by the MRI-guided CAD design process, closely mimics the human hand's natural ability to increase its span via finger abduction, which is commonly employed for grasping large or irregularly shaped objects. In addition, as shown in Figure 5G, hand adduction is also successfully achieved, with a 42.8% reduction in hand span when the index and little fingers are activated. Figure 5H and Movie S1, Supporting Information, demonstrate a series of "natural" movements, including partial and full hand closure, as well as everyday gestures involving the simultaneous closure or semiclosure of selected fingers while

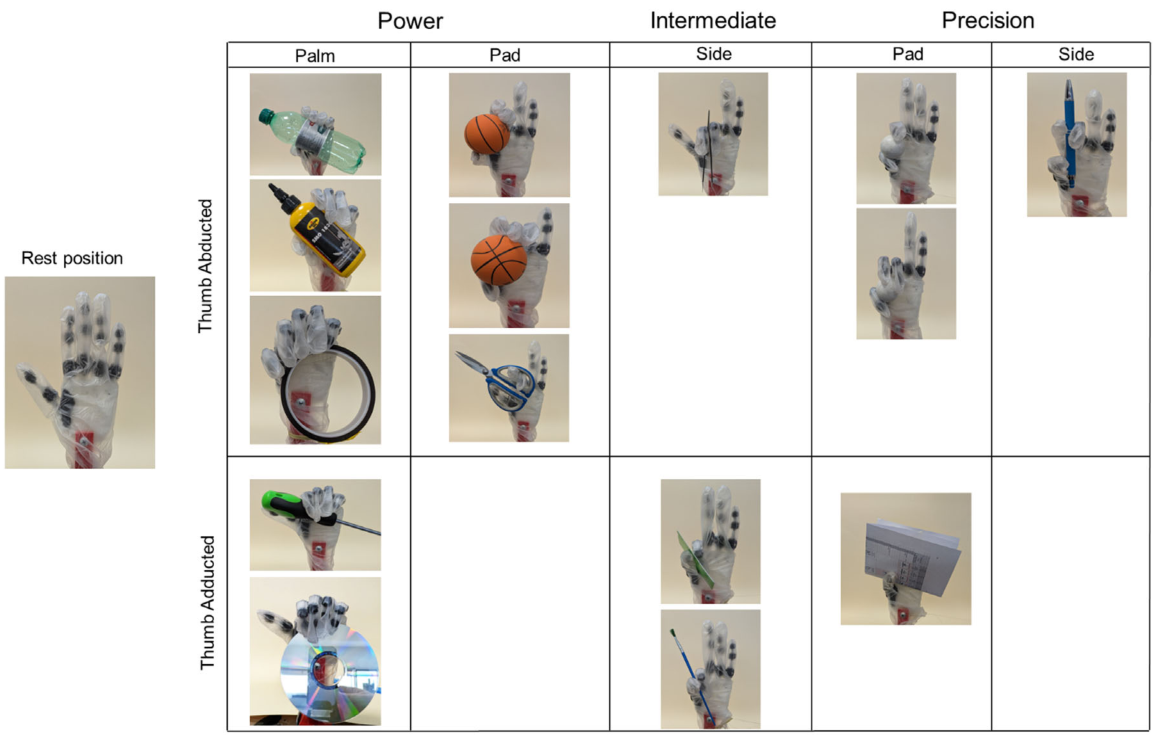

Figure 6. Feix test: Three types of grasps (power, intermediate, and precision), combining two thumb positions and three types of oppositions. A total of 12 objects were tested for a total of 15 grasping tasks.

keeping others inactive. This enables a wide range of movements used not only for grasping but also for expressive and communicative purposes.

The authors prioritized a novel desktop fabrication approach, guided by MRI data, over actuation technologies. Although not optimal, common stepper motors were used to facilitate a preliminary yet meaningful characterization of the device's performance. However, future works will focus on the integration of more appropriate artificial muscles. Figure 5I shows a comparison between commonly used actuation systems, in terms of stress, strain, and power density.

In addition to evaluating the grasping capabilities of the proposed 3D-printed hand, a simplified version of the test proposed by Feix[40] was conducted. Three types of grasps, classified as power, intermediate, and precision, were performed by combining two thumb positions (adducted and abducted) with three types of oppositions (palm, side, and pad) necessary to securely hold various objects. A total of 12 different objects were grasped, including flat items (e.g., paper, credit card), squeezable items (e.g., basketball), and small objects (e.g., brush, tweezer), for a total of 15 distinct grasping tasks. To increase the contact area during grasping, the hand was fitted with a transparent universal glove. **Figure 6** illustrates all the grasping modalities tested, demonstrating that the proposed hand is capable of grasping objects of various shapes and sizes and can perform a wide range of grasps, from pure power grasps to precise two-finger grips. Additionally, the maximum weight the hand could successfully grasp using a power grasp was evaluated. A 100% success rate (15 repetitions) was achieved when grasping objects weighing 0.5 and 1 kg (e.g., a bottle and a disk). When the weight increased to 1.5 kg, the success rate decreased to 86%, and for 2 kg objects, it further declined to 50%. These results suggest that the proposed 3D-printed hand can effectively grasp objects weighing up to 1.5–2 kg. Future work will focus on improving its ability to grasp heavier objects by incorporating features, such as artificial skin. Additionally, tendon sheaths will be incorporated into future designs, either by directly fabricating smooth sheaths over the fingers and the palm, or incorporating external elements (i.e., silicone cylinders) leveraging the stop-and-go methods.

To further demonstrate the potential of the proposed digital fabrication framework, the finger was equipped with two 3D-printed sensors, both fabricated monolithically using the same 3D printing machine described above (JG Maker Artist D Pro, JG Maker, China). Details about sensor fabrication can be found in the Experimental Section. As illustrated in **Figure 7**, two types of sensors were fabricated: a piezoresistive sensor for proprioception and a capacitive sensor for exteroception. The piezoresistive sensor was characterized by varying the finger's bending angle; the greater the bending, the higher the resistance change, with a sensitivity of 4.4 Ω/degree. The piezoresistive sensor was tested by performing a total of 10 consecutive bending cycles for every bending configuration (a total of five different configurations) at a frequency of 1 Hz. The capacitive sensor consisted of three main components, as shown in Figure 7A: two electrodes made

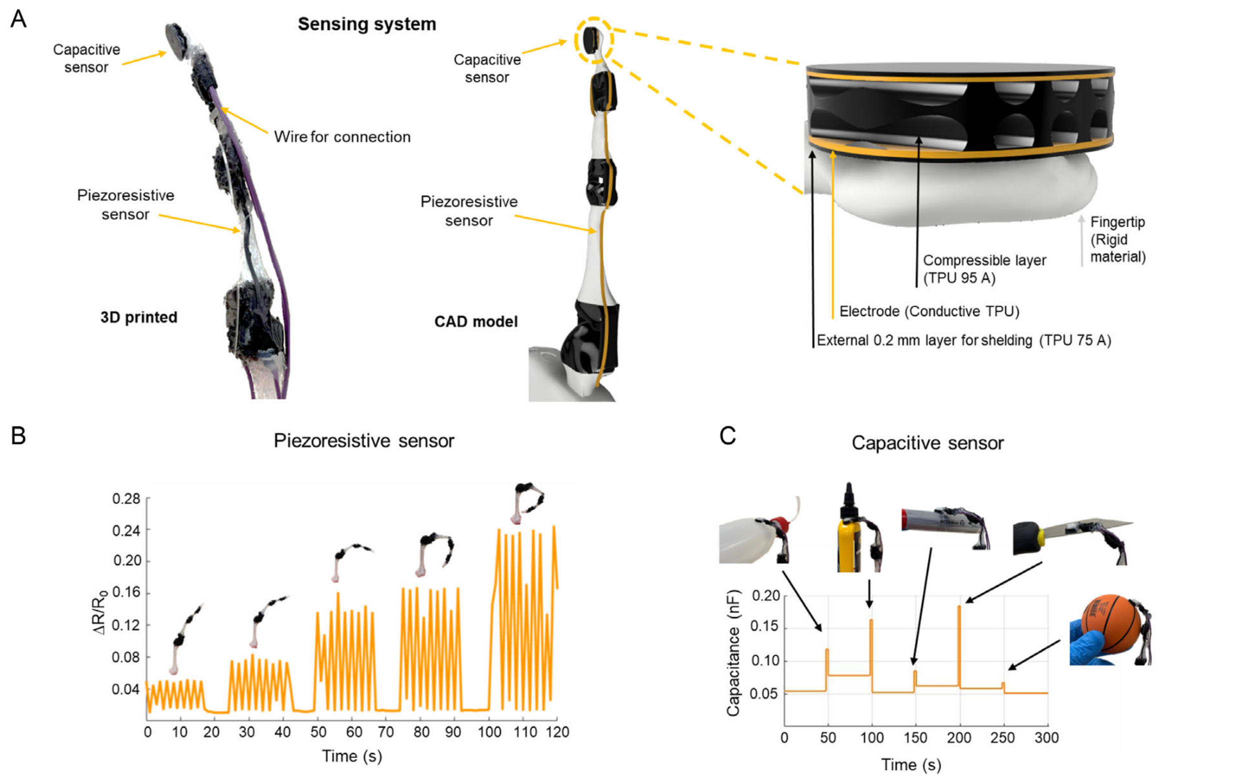

Figure 7. 3D-printed sensors: A) Actual 3D-printed finger and CAD model of the bioinspired finger with piezoresistive and capacitive sensors; B) piezoresistive sensor, direct correlation between change in resistance and bending angle of the finger; and C) capacitive sensor: change in capacitance when touching different objects.

of conductive TPU, a compressible separator based on a 20% density gyroid structure (TPU 75 A), and two insulating layers (TPU 75 A) to shield the electrodes from the external environment. This capacitive sensor was tested by subjecting the finger to impacts against various objects, simulating real-world object-approaching and grasping scenarios. As shown in Figure 7X, the sensor exhibited varying changes in capacitance depending on the object, due to the compression of the separator layer, which altered the distance between the electrodes. These changes in capacitance were influenced by several factors, including the object's surface characteristics and the nature of the impact.

Overall, these results demonstrate that the proposed fabrication approach can effectively integrate sensing capabilities into the musculoskeletal system. Future work will aim to optimize sensor placement within the finger or hand to enhance output and performance. This advancement paves the way for closed-loop control strategies, where sensors and actuators work in tandem to enable precise and controllable movements.

3. Discussion and Conclusions

In the present research, a framework for one-shot desktop 3D printing human-like hands with enhanced biomimicry is presented. The proposed method offers a unique approach compared to existing scientific literature by enabling the assembly-free and cost-effective (3D printer setup costs ≈€ 500) desktop 3D printing of highly biomimetic hands. In contrast, achieving high biomimicry in current research typically requires either expensive 3D printing methods, such as MJ or multiple assembly steps. Moreover, while some monolithic 3D printing approaches have been explored, they are associated with high costs due to MJ systems (>€ 10 000) or result in designs with very low levels of biomimicry. Additionally, the proposed approach is MRI-guided: MRI data has been processed to create CAD models of human hands, including key components (i.e., volar plate and collateral ligaments) tailored to the specifics of the patient. An adhesion-centered metric was used to select the soft and rigid materials for joints and bones, in conjunction with a gradient generation technique to create a bioinspired soft–stiff transition at the interface. Additionally, the finger was engineered with an embedded 3D interlocking, unlocked by multi-MEX 3D printing, increasing the adhesion at the soft–stiff interface by 293% (compared to plain interfaces). The proposed hand is equipped with two key biological features often overlooked in robotic hands: the volar plate and collateral ligaments. Such elements not only increase the biomimetic degree of the hand but are also responsible for enhancing the functionalities of every single finger, resembling human counterparts. In particular, the volar plate ensures proper bending of the finger only in the dorsal direction, acting as a constraint on the palmar side to prevent abnormal hyperextension. This behavior is reflected in two distinct values of stiffness of the proposed finger: dorsal and palmar stiffness of 68.5 and 114.9 $N\,m^{-1}$ were obtained. The collateral ligament enhances joint stability by absorbing stress from radial forces, preventing sideways motion during bending. These biomimetic features, combined with the high geometrical fidelity of the 3D-printed hand, enable a wide range of human-like behaviors. These capabilities include multiple bending angles of each finger, hand abduction that nearly doubles the hand span, hand adduction reducing the hand span of 42%, and an opposable thumb that moves across the palm to interact with all four fingers (thumb tip to fingertip contact), scoring a maximum of 10 out of 10 when performing Kapanjii test. The hand also exhibits highly repeatable motion patterns. Grasping performance was evaluated, demonstrating the ability to perform power, intermediate, and precision grasps using different thumb configurations (abducted and adducted) and opposition types (palm, side, and pad), mimicking the versatility of the human hand.

Further studies will focus on improving the actuation of the hand, in terms of a biomimetic approach: as the main focus of this article is providing a new fabrication paradigm, commercial stepper motors have been used. Artificial muscles, due to their compatibility with the proposed manufacturing method,[41] and to some intrinsic features such as stiffness, free strain, blocking stress, actuation frequency, and power usage, are ideal for replacing stepper motors. We have explored high-performance artificial muscles that have a power density in the range of 10^5–10^7 $J\,m^{-3}$[42] such as twisted and coiled polymer (TCP) muscles[43,44] and SMA[17,41] incorporated in robotic and orthotic hands with few joints' degree of freedom. The usage of nanomaterials-coated TCP muscles has also been proven to increase the power efficiency.[45] All these novel actuation technologies will be studied and integrated into the proposed hand in future work.

Additionally, the authors demonstrated the feasibility of directly 3D printing both piezoresistive and capacitive sensors, without requiring manual assembly, to equip the finger with proprioceptive and exteroceptive sensing capabilities. These low-cost sensors pave the way for closed-loop control strategies, as they can operate in tandem with actuators to dynamically achieve targeted outputs. To further improve biomimicry (and functionality), future works will focus on integrating functional elements, such as tendon sheaths and artificial skin.

The capabilities demonstrated by the proposed 3D-printed hand are a direct result of the MRI-guided design process, which facilitated the integration of critical anatomical elements. This approach is envisioned to be applied to the 3D printing of prosthetic and humanoid hands tailored to patient-specific requirements. The proposed MRI-to-3D-print framework integrates anatomical fidelity, functional architecture, and manufacturability into a streamlined, semiautomated process, marking a significant advancement toward intelligent digital fabrication of musculoskeletal systems characterized by improved performance as a direct consequence of the proposed 1) soft–stiff adhesion strategy, 2) MRI-guided inclusion of overlooked functional elements, and 3) possibility to process dissimilar materials in the same print.

Moreover, this method has the potential to serve as a foundation for the broader adoption of the "scan-and-print" technique, extending beyond hands to other parts of the musculoskeletal system. By leveraging this approach, various soft–stiff systems could be scanned and stored as MRI data, creating digital twins (CAD models) that can be utilized on demand. The proposed framework aims at enhancing prosthetics by enabling extreme personalization and ensuring optimal anatomical and functional compatibility. Integrating scan data into personal digital twins will allow continuous updates with new medical information, enabling prosthetics to adapt seamlessly to changes such as growth, muscle atrophy, or other health conditions. Additionally, increased production efficiency and reduced postoperative complications promise substantial long-term cost savings for healthcare systems and patients.

4. Experimental Section

From MRI to CAD Design: The open-access hand-focused MRI dataset provided by the University of Southern California (USC) served as the source for the MRI data used in this study (Acknowledgment section). Specifically, Subject 03 (male, 183 cm tall, 89 kg) was selected to create the hand model. The dataset includes 12 distinct hand poses, with 304 images per pose, each characterized by a slice thickness of 1 mm and an overlap of 0.5 mm (detailed scanning parameters are available on the dataset website). The MRI data were processed using the open-source 3D Slicer 5.6.2 software with semiautomatic thresholding and manual corrections, which allowed for balancing automation with precision in capturing small-scale features. Noise was reduced using filtering techniques, followed by both manual and semiautomated segmentation to assign distinct labels to each region of interest. Nonetheless, due to limitations in MRI resolution, some degree of simplification was necessary. For instance, extremely thin ligaments and some complex joint surface textures were either slightly smoothed or thickened in the CAD model to ensure they could be 3D printed. A 3D mesh model was then reconstructed, generating an OBJ file. This triangular mesh model was further refined in the open-source MeshLab software, where the mesh was edited, reconstructed, and healed to ensure continuity and smoothness. Subsequently, the model was imported into Fusion 360 (Autodesk, USA) and converted into a T-spline model. At this stage, the CAD design was engineered by 1) adding 3D-embedded interlocking mechanisms at the interface between joints and bones, 2) creating slots into the bones where embed the tendons, and 3) performing Design for (DfAM) by considering all the constraints of the multi-MEX 3D printer used throughout the present research, such as 3D printer resolution. The total price of the device and material consumption (for every finger) is detailed in Section S1, Supporting Information; however, the final hand is composed of a total of 29 parts, 3D printed in one shot. This workflow ensured that the resulting CAD design accurately replicated the anatomical structure while being optimized for fabrication.

Multimaterial 3D Printing: A commercial-grade multi-MEX 3D printer (JG Maker Artist D Pro, JG Maker, China) was employed. The Ultimaker Cura 5.9 slicing software was employed to set process parameters and generate G-code files. Throughout the whole research, a layer height of 0.1 mm was set, in conjunction with a nozzle size of 0.4 mm for high-resolution features. Smaller nozzles (e.g., 0.25 mm) were avoided due to compatibility issues with the soft material, which posed a high risk of clogging. The primary process parameters for each material are detailed in Section S2, Supporting Information. The start-and-stop method[46–48] was used to embed nylon fishing cords (diameter of 0.4 mm) acting as tendons, in every finger by dynamically (and automatically) pausing the 3D printing process and resuming it. A printing orientation minimizing the usage of the support was selected to enhance efficiency (Section S2, Supporting Information). After the 3D printing process, the only manual task required was the removal of supports. Notably, the use of hydrosoluble supports could further streamline the process if an MEX setup capable of extruding at least three materials were used,[49] thereby eliminating human intervention entirely.

Gradient Generation Technique: The proposed gradient generation method aims to create a soft–stiff material transition at the interface solely by leveraging the capabilities of a 3D printing machine, without requiring any hardware modifications. This technique involves two sequential steps in each printed layer: 1) extruding soft material over the already extruded stiff material to form an overlap and 2) ironing the gradient zone with the hot nozzle to enhance adhesion, as demonstrated in refs. [33,50]. The layer-by-layer process follows these steps: 1) first, the rigid material was extruded; 2) next, the soft material was deposited, forming a plain soft–stiff interface; 3) at the interface, an additional 0.4 mm-wide line of soft material was extruded, overlapping the stiff material by 0.2 mm, through.gcode modification; 4) after creating this overlap region (volume of 5.92 mm^3), the ironing process is performed by passing the hot nozzle in a zig-zag pattern over the overlap area without extruding material; and 5) ironing reheats the already extruded material while applying pressure, flattening the overlap, increasing wetting area and mixing the two materials. In this way, the soft material diffuses into the rigid one by creating a strain gradient. This process is repeated after every layer. Through a trial-and-error approach, various ironing distances (gap between the nozzle tip and the ironing area) were tested. The highest adhesion improvement (+38.7%) was achieved when the nozzle was lowered by 0.1 mm into the graded region. A low ironing speed of 5 mm s^{-1} was used to ensure uniform ironing. Both ironing parameters and interface overlap extrusions were incorporated by modifying the .gcode file.

Adhesion at the Soft–Stiff Interface: To evaluate the interface adhesion between soft and stiff materials, the ASTM D638 standard was followed. Specifically, Type IV samples were 3D printed, with the sample divided longitudinally: half composed of stiff material and the other half of soft material. A traverse speed of 5 mm min^{-1} was employed during testing.

For each material combination, three repetitions were fabricated and tested to account for variability. The testing was conducted using a universal testing machine (INSTRON 34TM10, Instron, USA) equipped with a 100 N load cell with a resolution of 0.1 N. The UTS, the maximum strength observed during the tensile test, was adopted as the adhesion metrics, consistent with scientific literature.[51,52]

The same universal testing machine was employed to perform low-frequency fatigue tests under both tensile and flexural loading. The cyclic tensile test was conducted at a frequency of 0.5 Hz using Type IV specimens in accordance with ASTM D638. The machine was programmed to impose a 20% tensile strain in each cycle, for a total of 10 000 cycles. The cyclic flexural test was also carried out at 0.5 Hz, using a three-point bending configuration following the ASTM D790 standard. The test specimen consisted of a rigid segment and a soft segment, with the soft–stiff interface positioned at the mid-span. A maximum flexural strain of 20% was applied per cycle, for a total of 10 000 cycles.

Testing Volar Plate and Collateral Ligament Effect: A universal testing machine (INSTRON 34TM10, Instron, USA) was used to test the effect of the volar plate on the finger displacement. A 3D-printed custom-made holder (reproducing in negative the metacarpus geometry) was employed to secure the finger while applying force. Three tests for configurations were performed: in the first configuration, the force was applied on the dorsal side, in the second configuration, the finger was flipped, and the force was applied on the palmar side (see Figure 4). The force was applied by means of a metallic indenter, used for 3- and 4-point bending testing. It should be noted that the force was locally applied as depicted in Figure 4A, B. A traverse speed of 5 mm min^{-1} was set. The testing machine was equipped with a 100 N load cell. A Canon EOS 4000D camera (Canon, Japan) was positioned in front of the sample, aligned parallelly to the finger, to record the test. A red marker on the tip of the finger was used to ease displacement tracking. The displacement was automatically analyzed using the Tracker software (OSP – Open Source Physics, USA). The same workflow was applied to test the collateral ligament, with the key difference being the force application point. For this test, force was applied to the radial side rather than the dorsal or palmar side.

Actuation of the Finger/hand, Blocking Force, and Grasping: As previously introduced, nylon tendons (0.4 mm diameter) were manually embedded during the 3D printing process (start-and-stop approach). Each finger (except the thumb) was equipped with four tendons: three flexor tendons on the dorsal side near the three joints, and one extensor tendon on the palmar side near the middle phalanx, mimicking the human anatomy. These tendons were connected to NEMA 17 stepper motors, controlled via Arduino (see Section S5, Supporting Information).

The primary setup for measuring blocking force utilized a commercial force sensor and an Arduino board (details in Section S7, Supporting Information).

D Printing Sensors: The finger was equipped with two sensors: a piezoresistive and a capacitive sensor, providing proprioception and exteroception, respectively. Both sensors were fabricated by 3D printing a commercially available electrically conductive TPU (Ninjatek Eel, Ninjatek, USA). Although the 3D printer used in this study featured only two print heads, a custom G-code modification enabled the deposition of three distinct materials (rigid, soft, and electrically conductive) within a single print. This was achieved by dynamically unloading one material and loading the next, as instructed via the G-code. To prevent cross-contamination, 100 mm of the new material were extruded in free air (at the left corner of the print bed), following each material switch to fully purge the nozzle. While the extrusion of three materials with a dual-head setup proved feasible, it was both time- and material-intensive. This limitation could be effectively addressed by employing a multihead printer with a tool-changing architecture, such as those offered by Prusa Research, Czech Republic, which remain inexpensive (under €5,000).

Supporting Information

Supporting Information is available from the Wiley Online Library or from the author.

Acknowledgements

Bohan Wang, George Matcuk, Jernej Barbic: Hand MRI dataset, University of Southern California, 2020. http://www.jernejbarbic.com/hand-mri-dataset. BRIEF—Biorobotics Research and Innovation Engineering Facilities—Missione 4, 'Istruzione e Ricerca'—Componente 2, 'Dalla ricerca all'impresa'—Linea di investimento 3.1, 'Fondo per la realizzazione di un sistema integrato di infrastrutture di ricerca e innovazione', funded by European Union—NextGenerationEU, CUP: J13C22000400007. Italian Ministry of University and Research under the Programme "Department of Excellence" Legge 232/2016 (Grant No. CUP - D93C23000100001) National Institutes of Health grant U12AB123456 (PV, CHO)

Conflict of Interest

The authors declare no conflict of interest.

Author Contributions

Gianni Stano: conceptualization; investigation; writing—original draft; writing—review and editing. **Matteo Cianchetti**: conceptualization; supervision; writing—original draft; writing—review and editing. **Antonio Pavone**: methodology; investigation; visualization; writing—original draft; writing—review and editing. **Mattia D'Orazio**: methodology; investigation; visualization. **Yonas Tadesse**: supervision; writing—original draft; writing—review and editing. **Gianluca Percoco**: conceptualization; supervision; writing—original draft; writing—review and editing.

Data Availability Statement

The data that support the findings of this study are available in the supplementary material of this article.

Keywords

biomimetic hands, desktop multimaterial 3D printing, hybrid robotics, one-shot additive manufacturing, prosthetics

Received: April 28, 2025
Revised: June 23, 2025
Published online:

[1] J. Park, M. Chang, I. Jung, H. Lee, K. Cho, *Adv. Intell. Syst.* **2024**, *6*, https://doi.org/10.1002/aisy.202300607.
[2] M. R. Aryal, S. Pun, *Int. J. Interact. Des. Manuf.* **2022**, *16*, 1099.
[3] H. Moeinnia, H. Su, W. S. Kim, *Adv. Intell. Syst.* **2022**, *4*, https://doi.org/10.1002/aisy.202200189.
[4] L. Zhou, L. Ren, Y. Chen, S. Niu, Z. Han, L. Ren, *Adv. Sci.* **2021**, *8*, 1.
[5] Y. Liu, C. Yiu, Z. Song, Y. Huang, K. Yao, T. Wong, J. Zhou, L. Zhao, X. Huang, S. K. Nejad, M. Wu, D. Li, J. He, X. Guo, J. Yu, X. Feng, Z. Xie, X. Yu, *Sci. Adv.* **2022**, *8*, 1.
[6] Y. Song, R. Y. Tay, J. Li, C. Xu, J. Min, E. S. Sani, G. Kim, W. Heng, I. Kim, W. Gao, *Sci. Adv.* **2023**, *9*, 1.
[7] H. Zhao, K. O'Brien, S. Li, R. F. Shepherd, *Sci. Rob.* **2016**, *1*, 1.
[8] M. Ortiz-Catalan, J. Zbinden, J. Millenaar, D. D'Accolti, M. Controzzi, F. Clemente, L. Cappello, E. J. Earley, E. Mastinu, J. Kolankowska, M. Munoz-Novoa, S. Jönsson, C. Cipriani, P. Sassu, R. Brånemark, *Sci. Rob.* **2023**, *8*, 1.
[9] S. Terryn, J. Brancart, D. Lefeber, G. Van Assche, B. Vanderborght, *Sci. Rob.* **2017**, *2*, 1.
[10] Y. Jung, K. Kwon, J. Lee, S. H. Ko, *Nat. Commun.* **2024**, *15*, 1.
[11] M. Smith, V. Cacucciolo, H. Shea, *Science* **2023**, *379*, 1327.
[12] J. S. Cuellar, G. Smit, D. Plettenburg, A. Zadpoor, *Addit. Manuf.* **2018**, *21*, 150.
[13] K. Lussenburg, A. Sakes, P. Breedveld, *Addit. Manuf.* **2021**, *39*, https://doi.org/10.1016/j.addma.2021.101846.
[14] R. Mutlu, G. Alici, M. In het Panhuis, G. M. Spinks, *Soft Rob.* **2016**, *3*, 120.
[15] A. Mohammadi, J. Lavranos, H. Zhou, R. Mutlu, G. Alici, Y. Tan, P. Choong, D. Oetomo, *PLoS One* **2020**, *15*, https://doi.org/10.1371/journal.pone.0232766.
[16] H. Zhou, C. Tawk, G. Alici, *IEEE Trans. Neural Syst. Rehabil. Eng.* **2022**, *30*, 550.
[17] E. Deng, Y. Tadesse, *Actuators* **2021**, *10*, 1.
[18] J. S. Cuellar, G. Smit, P. Breedveld, A. A. Zadpoor, D. Plettenburg, *Proc. Inst. Mech. Eng., Part H* **2019**, *233*, 1122.
[19] C. De Pascali, G. A. Naselli, S. Palagi, R. B. N. Scharff, B. Mazzolai, *Sci. Rob.* **2022**, *7*, https://doi.org/10.1126/scirobotics.abn4155.
[20] Z. Xu, E. Todorov, in *Proc. IEEE Int. Conf. Robotics and Automation (ICRA)*, June 2016, pp. 3485–3492.
[21] L. Tian, J. Zheng, Y. Cai, M. F. K. B. A. Halil, N. M. Thalmann, D. Thalmann, H. Li, *Int. J. Bioprint.* **2022**, *8*, 1.
[22] J. A. E. Hughes, P. Maiolino, F. Iida, *Sci. Rob.* **2018**, *3*, 1.
[23] T. J. K. Buchner, S. Rogler, S. Weirich, Y. Armati, B. G. Cangan, J. Ramos, S. T. Twiddy, D. M. Marini, A. Weber, D. Chen, G. Ellson, J. Jacob, W. Zengerle, D. Katalichenko, C. Keny, W. Matusik, R. K. Katzschmann, *Nature* **2023**, *623*, 522.
[24] M. Koot, N. Sauer, T. Fenton, *J. Forensic Sci.* **2005**, *50*, JFS2004229-6.
[25] S. E. Naleway, M. M. Porter, J. McKittrick, M. A. Meyers, *Adv. Mater.* **2015**, *27*, 5455.
[26] F. Barthelat, Z. Yin, M. J. Buehler, *Nat. Rev. Mater.* **2016**, *1*, 1.
[27] S. Hasanov, A. Gupta, A. Nasirov, I. Fidan, *J. Manuf. Processes* **2020**, *58*, 923.
[28] G. Stano, S. M. A. I. Ovy, G. Percoco, R. Zhang, H. Lu, Y. Tadesse, *3D Print. Addit. Manuf.* **2023**, *10*, 1080.
[29] U. Altuntas, D. Coker, D. Yavas, *Addit. Manuf.* **2023**, *61*, 103359.
[30] J. T. Green, I. A. Rybak, J. J. Slager, M. Lopez, Z. Chanoi, C. M. Stewart, R. V. Gonzalez, *Addit. Manuf. Lett.* **2023**, *7*, 100177.
[31] D. C. Ames, S. Propst, A. Shah, J. Mueller, *Adv. Mater.* **2024**, *36*, 2407599.
[32] S. J. Ahn, H. Lee, K. J. Cho, *Nat. Commun.* **2024**, *15*, 1.
[33] G. Stano, A. Pavone, M. A. Jafor, K. Matalgah, G. Percoco, T. J. Fleck, *Virtual Phys. Prototyping* **2024**, *19*, https://doi.org/10.1080/17452759.2024.2331153.

[34] T. J. Coogan, D. O. Kazmer, *Rapid Prototyping J.* **2017**, *23*, 551.
[35] T. J. Coogan, D. O. Kazmer, *Addit. Manuf.* **2020**, *35*, 101368.
[36] M. C. Saldívar, E. Tay, A. Isaakidou, V. Moosabeiki, L. E. Fratila-Apachitei, E. L. Doubrovski, M. J. Mirzaali, A. A. Zadpoor, *Nat. Commun.* **2023**, *14*, 1.
[37] C. Darkes-Burkey, R. F. Shepherd, *Adv. Mater.* **2024**, *36*, 1.
[38] S. Saito, Y. Suzuki, *J. Hand Surg., Am.* **2011**, *36*, 265.
[39] A. Pérez-González, M. Vergara, J. L. Sancho-Bru, *J. Biomech.* **2013**, *46*, 2644.
[40] T. Feix, J. Romero, H. B. Schmiedmayer, A. M. Dollar, D. Kragic, *IEEE Trans. Hum.-Mach. Syst.* **2016**, *46*, 66.
[41] G. Stano, S. M. A. I. Ovy, J. R. Edwards, M. Cianchetti, G. Percoco, Y. Tadesse, *Int. J. Adv. Manuf. Technol.* **2023**, *124*, 467.
[42] Y. Tadesse, L. Wu, L. K. Saharan, *Mech. Eng.* **2016**, *138*, 11.
[43] L. Wu, M. Jung De Andrade, L. K. Saharan, R. S. Rome, R. H. Baughman, Y. Tadesse, *Bioinspiration Biomimetics* **2017**, *12*, 026004.
[44] L. Saharan, M. J. De Andrade, W. Saleem, R. H. Baughman, Y. Tadesse, *Smart Mater. Struct.* **2017**, *26*, https://doi.org/10.1088/1361-665X/aa8929.
[45] P. S. Matharu, Y. Song, U. Gandhi, *Biomimetics* **2024**, *9*, 458.
[46] E. MacDonald, R. Salas, D. Espalin, M. Perez, E. Aguilera, D. Muse, R. B. Wicker, *IEEE Access* **2014**, *2*, 234.
[47] D. Espalin, D. W. Muse, E. MacDonald, R. B. Wicker, *Int. J. Adv. Manuf. Technol.* **2014**, *72*, 963.
[48] E. MacDonald, R. Wicker, *Science* **2016**, *353*, https://doi.org/10.1126/science.aaf2093.
[49] J. Cañada, H. Kim, L. F. Velásquez-García, *Virtual Phys. Prototyping* **2024**, *19*, https://doi.org/10.1080/17452759.2024.2310046.
[50] G. Stano, N. Sayah, D. E. Smith, T. J. Fleck, *Addit. Manuf. Lett.* **2024**, *9*, 100194.
[51] T. Kuipers, R. Su, J. Wu, C. C. L. Wang, *Addit. Manuf.* **2022**, *50*, 102495.
[52] M. Ribeiro, O. Sousa Carneiro, A. Ferreira da Silva, *Rapid Prototyping J.* **2019**, *25*, 38.